An energy efficient way for quantitative magnetization switching

Check for updates

Xin Li[1,7], Hanuman Singh[2,7], Jie Lin[1], Shuai Zhang[1], Bao Yi[1], Jyotirmoy Chatterjee[3], Zhuyun Xiao[4], Sucheta Mondal[2], Nobumichi Tamura[5], Rob N. Candler[4], Long You[1], Jeffrey Bokor[2] & Jeongmin Hong[2,6] ✉

Recent advancements in electrically controlled spin devices have been made possible through the use of multiferroic systems comprising ferroelectric (FE) and ferromagnetic (FM) materials. This progress provides a promising avenue for developing energy-efficient devices that allow for electrically controlled magnetization switching. In this study, we fabricated spin orbit torque (SOT) devices using multiferroic composites and examined the angular dependence of SOT effects on localized in-plane strain induced by an out-of-plane electric field applied to the piezoelectric substrate. The induced strain precisely modulates magnetization switching via the SOT effect in multiferroic heterostructures, which also exhibit remarkable capability to modulate strain along different orientations – a feature with great potential for future applications in logic device arrays. To investigate the influence of electric fields on magnetization switching, harmonic Hall measurements, synchrotron-powered x-ray magnetic circular dichroism-photoemission electron microscopy (XMCD-PEEM), x-ray diffraction (XRD), magnetic force microscopy (MFM), and micromagnetic simulation were conducted. The results demonstrate that electric-field-induced strain enables precise control of SOT-induced magnetization switching with significantly reduced energy consumption, making it highly suitable for next-generation spin logic devices.

Spintronics has vast potential for a wide range of applications, such as neuromorphic computing, flexible spintronic devices, quantum computing, radiation-tolerant devices, memory storage, and sensors[1–9]. In these devices, the surface and interface characteristics strongly influence the spin transport[10,11]. The potential of multiferroic materials in energy conversion and novel spintronic devices has captured the attention of researchers[12–16]. However, single-phase multiferroic material, such as BiFeO₃(BFO), remains limited in its potential. Polarization arises from ion displacement from centered positions in single-phase ferroelectric material enabling stable states with fully occupied or empty orbitals while magnetic order is achieved through ordered electron spins in partially filled orbitals[17].

Multiferroic heterostructures also known as artificial multiferroics offer a means of achieving this energy conversion at room temperature by providing an interface between multiple materials that exhibit distinct properties of ferromagnetism and ferroelectricity[18,19]. Spin-orbit torque (SOT) has garnered significant attention because of its exceptional performance which makes it efficient due to nonvolatility, high speed, low power dissipation, and good compatibility with the well-established

semiconductor or devices[20–24]. SOT-based magnetization switching has been demonstrated as an efficient and speedy device in terms of write/read time and energy consumption with nonvolatility, high speed, low power dissipation, and good compatibility with well-established semiconductor devices[22–24]. Two mechanisms of SOT are the Rashba effect and spin hall effect (SHE), generated at the interface of magnetic heterostructures with broken inversion symmetry and from bulk spin-orbit coupling respectively[25].

Pioneering experimental studies have proposed the existence of sizeable damping-like (or Slonczewski) torque (DLT)[26,27] with $\vec{m} \times (\vec{m} \times \vec{p})$ and field-like torque (FLT)[28] with $\vec{m} \times \vec{p}$ in ferromagnet/heavy metal (FM/HM) bilayers where magnetization direction is represented by $\vec{m}$ while polarization is represented by $\vec{p}$, respectively. represent the directions of the magnetization and polarization of the spin current, respectively. DLT and FLT are the most significant torques for magnetization switching. Nevertheless, the relative contribution of these two kinds of SOTs in a variety of device structures is still under sufficient discussion. The roles of DLT and FLT have been extensively explored in HM[29–31]. The fabrication of Ta-based

¹School of Sciences, Hubei University of Technology, Wuhan 430068, China. ²EECS, UC Berkeley, Berkeley, CA 94720, USA. ³IMEC, Leuven 3001, Belgium. ⁴Department of Electrical Engineering UCLA, Los Angeles, CA 90095, USA. ⁵Advanced Light Source, LBNL, Berkeley, CA 94720, USA. ⁶School of Integrated Circuits, Huazhong University of Science and Technology, Wuhan 430074, China. ⁷These authors contributed equally: Xin Li, Hanuman Singh. ✉e-mail: jehong@berkeley.edu

SOT devices was conducted in this study for the purpose of comparing their DLT and FLT magnitudes[31].

Manipulation of SOTs could help control the magnetic transport behaviors in FM/HM heterostructure[32,33]. In addition to current-induced magnetization switching, multiferroic heterostructures offer more efficient ways of utilizing electric field-induced strain to control magnetization switching[34–41]. Specifically, the use of locally generated strains in simplified device architectures allows for an additional degree of control of magnetic spin-switching. Thus, SOT offers a competitive technology in the development of the next generation of information devices[41,42].

This work investigates Ta/CoFeB multilayers on a PMN-PT substrate that was fabricated for tuning SOTs by applying an electric field perpendicular to piezoelectric substrates inducing an in-plane strain measurement using harmonic hall voltage measurements. The angular dependence study shows how effective fields vary depending on piezoelectric substrate orientation. DLT's effective field was found linearly manipulable via the strain direction. The architecture of spintronics logic devices based on SOT and piezoelectric regulation offers the potential to implement complete Boolean logic functions, while also being proposed with ultralow energy consumption.

Results and Discussion

To investigate this study, we performed magnetization switching with the help of strain verified using PEEM, X-ray micro diffraction, MFM and micromagnetic simulation as the following section.

As shown in Fig. 1a, (011) oriented single crystal PMN-PT substrate, with a thickness of 500 μm, is double-side polished and covered by Pt electrodes on both top and bottom surfaces. Before depositing the magnetic layers on top of the substrate, PMN-PT is electrically pre-poled in [011] direction, with the polarization pointing "up". Under a vertically applied electric field, the PMN-PT substrate exhibits an anisotropic in-plane piezoelectric response, inducing compressive strain in the [100] direction and tensile strain in the [0$\bar{1}$1] direction. The SOT devices are lithographically fabricated into a Hall bar structure. Devices with different orientations are designed to verify the angular dependence of SOT efficiency manipulation, as shown in the sample picture in Fig. 1b. The external magnetic field response of the CoFeB/PMN−PT heterostructure device has been characterized in Fig. 1c and d, which indicates that the system is in-plane magnetized.

Spin Transfer Torque-Ferromagnetic Resonance (ST-FMR), Magneto-optic Kerr effect (MOKE), and Second harmonic spin-torque magnetometry have been proposed for the precise quantification of current-induced torques in the heterostructure device. Among them, harmonic hall measurements[30,43,44] involves the application of an alternating current (AC) with a specific frequency to generate alternating torques. This process causes the magnetization of the ferromagnetic (FM) layer to periodically tilt around its homeostatic states. DLT and FLT can be separated according to the distinct dependencies on variations in magnetic field angle or magnitude. Notably, adjusting the in-plane magnetic field angle is particularly suitable for devices that exhibit in-plane magnetization or possess weak perpendicular magnetic anisotropy (PMA).

In the structure shown in Fig. 1a, a constant sinusoidal current $I(t) = I_0 \sin \omega t$ with frequency of $f = (\omega / 2\pi) = 133 Hz$ is applied to the Hall bar via a bias tee. Simultaneously, an orthogonal voltage $V_{xy} = R_{xy} \cdot I_0 \sin \omega t$ is detected by a lock-in amplifier (LIA). The Hall resistance primarily arises from the anomalous hall Effect (AHE) and the planar hall effect (PHE). The hall voltage signal can be expressed as the Eq. (1).

$$V_{xy} = I_0 \sin \omega t \times \begin{bmatrix} R_A(\cos\theta - \sin\theta \cdot \Delta\theta) + \\ R_P(\sin^2\theta + \sin 2\theta \cdot \Delta\theta)(\sin 2\varphi + 2\cos 2\varphi \cdot \Delta\varphi) \end{bmatrix}$$

(1)

Given that the external field rotates in XOY plane with an angle φ, and the direction of spin-polarized current is along (0,1,0) direction, the hall voltage signal can be simplified as Eq. (2).

$$V_{xy} = I_0 \sin \omega t \times \begin{bmatrix} R_P \sin 2\varphi - \\ R_A\left(-\frac{H_{DL}}{-H_K + H}\right)\sin\omega t + 2R_P \frac{H_{FL}}{H}\cos 2\varphi \cos\varphi \sin\omega t \end{bmatrix}$$

(2)

Among these,

$$V_{xy}^{1\omega} = I_0 \sin\omega t \times R_P \sin 2\varphi \qquad (3-a)$$

$$V_{xy}^{2\omega} = I_0 \sin\omega t \times \left(R_A \cdot \frac{H_{DL}}{-H_K + H}\cos\varphi + 2R_P \frac{H_{FL}}{H}\cos 2\varphi \cos\varphi\right)$$

(3-b)

Here, R_P, R_A represent the planar hall resistance and anomalous hall resistance, respectively. H_{FL}, H_{DL}, H_K, H represent the current induced effective field of FLT and DLT, effective perpendicular anisotropy field and external field, respectively. The first and second harmonic hall voltage curves under increasing magnetic field are shown in Fig. 1e and f.

The magnitude of FLT' and DLT' effective field can be determined by calculating the coefficient obtained from fitting the measured curves with the aforementioned functions. As shown in Fig. 1b, four different orientations, described as 0-, 45-, 90-, and 135-degree devices according to their current direction, are designed to experience different strain distributions originating from the piezoelectric substrates. The vertical electric field is applied on the piezoelectric substrates, where the top electrode is connected to the ground and the bottom electrode is connected to a positive high voltage ranging from 0 V to 400 V.

As shown in Fig. 2a, the effective field of DLT and FLT at zero electric fields is set as the baseline, and the deviations from this baseline under increasing electric fields are documented. Because of the electric field polarity and substrate orientation, compressive strain is exerted on the 0-degree device, while tensile strain is experienced by the 90-degree device. It is evident that compressive strain diminishes the effective field of DLT, whereas tensile strain enhances it. In the case of the 45- and 135-degree devices, the effective field of DLT continues to rise, suggesting that tensile strain governs the strain distribution in these cases. Conversely, the effective field of FLT remains nearly constant across different device orientations, as illustrated by the dashed line in Fig. 2a.

Micromagnetic simulation is also performed to validate and further analyze the measurement results. A multiferroic heterostructure is constructed in COMSOL Multiphysics to analyze the strain distribution in the ferromagnetic layer under an electric field. Subsequently, the model is implemented in the Object-Oriented Micromagnetic Framework (OOMMF) to showcase the magnetization dynamics influenced by the aforementioned strain[45]. Further details regarding the settings can be found in the Methods section. In Fig. 2b, the device is represented as a current path with two electrodes in the simulation setup. It is observed qualitatively that tensile strain affects the 0-degree device, while compressive strain impacts the 90-degree device, as depicted in the insets of Fig. 2b. For the 45-degree and 135-degree devices, predominantly tensile strain is observed, aligning with experimental findings.

As shown in Fig. 2b, magnetization precession of the FM layer is compared under two conditions, called "on (011) PMN-PT" and "without strain", which considered the strain induced by the electric field on (011) PMN-PT or not, in respectively. Three stages are observed, which are ① initial state, ② middle state following the influence of SOT current and magnetoelastic energy and ③ final state after relaxation, respectively. Snapshots of in-plane magnetization at each stage are shown in Fig. 2b. The magnetization direction of FM layer($\bar{M}$) along + x/-x are represented by red and blue color, average $\bar{M}$ of the device is shown by the black arrow in the middle of the bar. As additional evidence, magnetization dynamics of the FM layer in X-axis and Y-axis are shown in Fig. 2c, with the spin direction of the initial and final states indicated in the diagram.
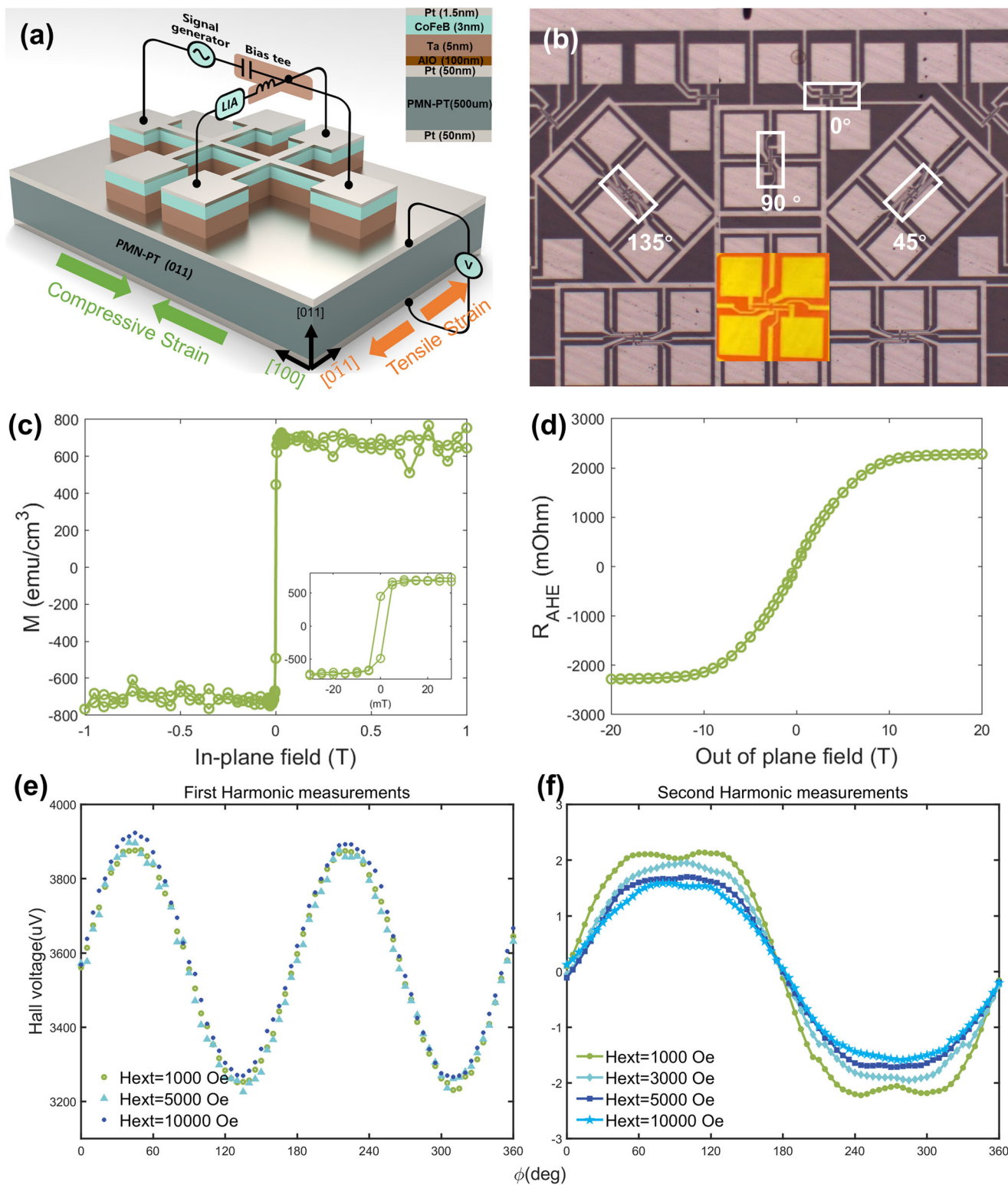
Fig. 1 | Experimental set up and transport measurements. a Schematic of Ta/CoFeB/Pt/PMN-PT/Pt heterostructure and the harmonic hall voltage testing method; **b** Devices are structured with the orientations of 0°, 45°, 90°, and 135° to measure angular dependence, details of the device is clearly shown in the insert; **c** Magnetic moment measurement of the devices under in-plane magnetic field, insert shows the M-H loop with external field varying from -30~30 mT; **d** Typical AHE curve of the device under out-of-plane magnetic field; **e** First and **f** Second harmonic hall voltage curves under increasing magnetic field.

In both scenarios mentioned above, a consistent current density of 5×10^{11} A/cm^2 was applied. Comparing the two cases with/without strain, it becomes evident that the magneto-elastic energy alone was insufficient to facilitate magnetization switching at final state in 0-degree case. However, in the cases of 45-, 90- and 135-degree, the magneto-elastic energy plays a crucial role in facilitating the magnetization switching[32,41,46,47]. It illustrates that, under the specified current density, in-plane strain assists the FM layer in achieving deliberate magnetization switching rather than random magnetization switching.
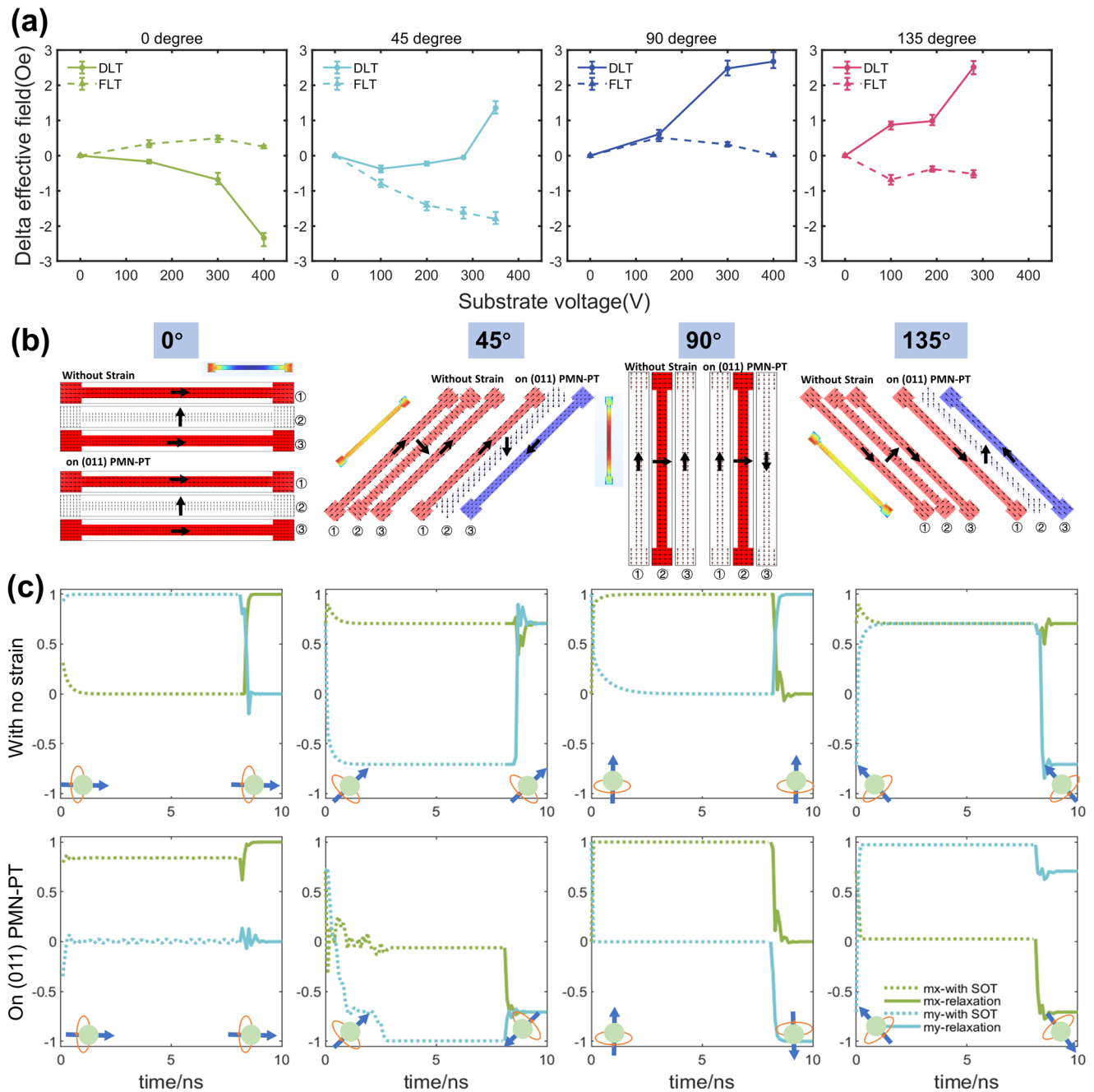
Fig. 2 | **Comparative studies of harmonic hall measurements and micromagnetic simulation. a** Harmonic Hall measurement results of devices aligned with the angle of 0, 45, 90, and 135 degrees, respectively. The effective field of DLT and FLT varied with the substrate voltage. **b**, **c** Strain distribution and magnetization switching process in FM layer of devices with four orientations. Two cases, without strain and with strain on (011) PMN-PT, are compared. We demonstrated different switching scenarios in two ways, which are the screenshot of in-plane magnetization and m_x, m_y varied with time, respectively.

The electric field-induced in-plane strain makes it possible to switch the magnetization with much lower energy consumption, which is around 200 fJ in one operation through estimation. In this study, we choose a type-x structure where the magnetization direction of ferromagnetic layers and the charge current direction are collinear without strain. We need an external symmetry-breaking effective field to facilities deterministic switching in type -x structure[46,47]. Here, the symmetry-breaking effective field is generated with the bi-directional strain produced by PMN-PT (011) with the applied electric field rather than an external magnetic field. Also, in straintronic logic devices, locally generated strain provides a way to write information to logic bits in selected area, thereby facilitating the implementation of specific logic functions[37,48].

The scenario of SOT operation in our device is shown in Fig. 3a. H_{DL}' and τ_{DL}' are effective fields and torque of DLT, which are compared to normal cases (H_{DL} and τ_{DL}), after electric field is applied on the substrate. Black arrows in top layer and bottom layer represent $\vec{M}$ and injected electron current, respectively.

MFM, X-ray microdiffraction, and PEEM were also adapted to help verify the electric field-assisted magnetization switching. More experimental details are described in Methods part. Figure 3b shows MFM results of the magnetization switching process of the CoFeB magnetic dot under four different excitation conditions. The magnetic dot with the diameter of 5 μm was fabricated here for better observation of magnetization switching. From the MFM pictures, it's not hard to find that, with strain only, partial
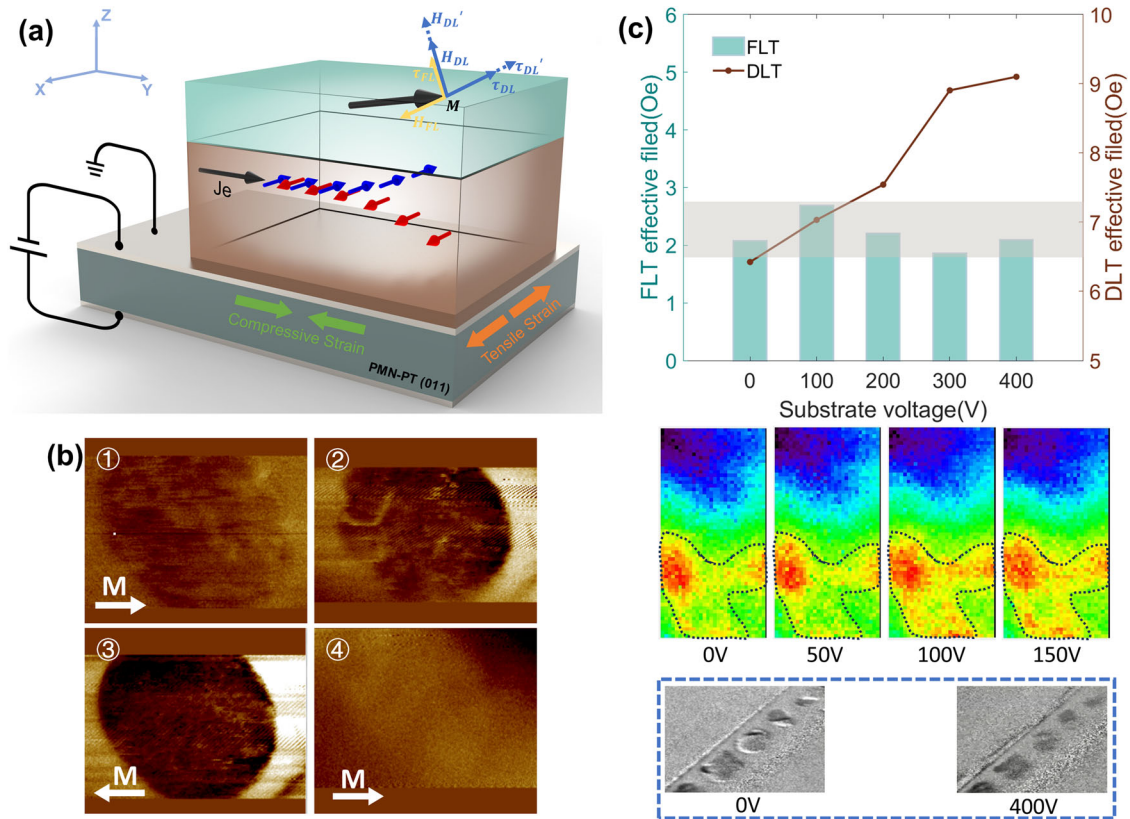
Fig. 3 | SOT coordinate system and its experimental results including MFM, PEEM, and x ray diffraction. a SOT operation scenario of the FM/HM/FE heterostructure. **b** MFM results of the magnetization switching process of the CoFeB magnetic dot. Four pictures indicate different stages, which are 1. with no current, no strain; 2. with strain only; 3. with strain and current; 4. strain with reverse current direction. **c** With the applied voltage increased, changing trend of the effective field of FLT and DLT, PEEM pictures of the magnetic dot as well as X-ray microdiffraction result of the device.

magnetization reversal occurs, while it is fully magnetized with both strain and current applied. In stage 4, with reverse strain and current direction, magnetization is switched back to the initial state. It can be observed that from stage 1 to 2, the strain applied help implement partial magnetization switching; from stage 2 to 3, current along with strain can help full magnetization switching. The MFM results verify that not only strain could help full magnetization switching, but also opposite current direction could help rewrite $\vec{M}$, which is essential for the information writing in storage technology.

As shown in Fig. 3c, effective fields of FLT and DLT under different substrate voltages are tested, and the effective field of DLT keeps increasing but that of FLT remains constant. Laue X-ray microdiffraction was used to investigate the elastic strain distribution on the heterojunction device. As shown in Fig. 3c, the X-ray microdiffraction results demonstrate that the strain increases (red region expanded) in the middle of the bar as the applied voltage increases. PEEM results demonstrate the magnetization switching on the magnetic dot when the substrate voltage ranges from 0 V to 400 V. It can be confirmed that the increasing effective field of DLT, which is caused by the electric field-induced in-plane strain, assists the magnetization switching.

Based on the comprehensive analysis of the aforementioned effective field data, PEEM, MFM, and X-ray microdiffraction results, we can deduce that the increase in in-plane strain caused by elevated substrate voltage is effectively transmitted to the FM layer. This contributes to an augmentation of the DLT effective field, which plays a supplementary role in achieving complete magnetization switching within the FM layer. Furthermore, these characterization findings align consistently with both the experimental observations and micromagnetic simulation outcomes depicted in Fig. 2.

As shown in Fig. 4a, three inputs (ends of arms) and three control parts (arms), as well as one output (connection) are integrated into a single logic

device. As the negation device and the buffer device are shown in Fig. 4b and c, an extra arm is designed to implement the function of buffer and negation. The original output called the middle is used to store the intermediate state of the FM layer. Magnetic tunnel junction (MTJ) stacks are designed at the input, middle, and output ends to readout the magnetization state of the FM layer. The logic state of each end is represented by the resistance state of the readout MTJ stack, which can be rewritten by the polarity of SOT current. Logic states of "0"/"1" represent low/high resistance states of the MTJ stack, respectively. Piezoelectric substrate PMN-PT (011) is designed under each arm of the logic unit for utilizing the strain to assist the magnetization switching. Serving as controlling parts, as well as buffer and negation controlling arms, strain is delivered to the FM layer through the protruding yellow part. In other areas, strain is impeded by the oxide material (represented by dark grey) to prevent the effect on the logic state of inputs/output MTJs. For the control and buffer/negation arms, their logic states of "0"/"1" represent the existence of strain, namely power-on/power-off of the electric field applied on the FM arm, respectively.

As a single logic unit shown in Fig. 4a, with three control ends setting as "1", "AND" and" OR", logic functions can be toggled in a reconfigurable way in the majority gate, as listed in the top half part of the truth table in Fig. 4d. Any two of the inputs selected can perform "AND" and" OR" operations. For the logic function of the selector shown in the bottom half, the result of the "AND" operation of the two inputs, which are set as "1" and the remaining one setting as "0", will be shown in the output. Therefore, control ends are able to select the inputs for logic operations.

Beyond that, data buffering and negation can be implemented in structures shown in Fig. 4b and c. According to the angular dependence of the magnetization switching, which has been described in the micromagnetic simulation section, with the same magnitude of current density as well as electric field applied on the logic device, the magnetization state of the
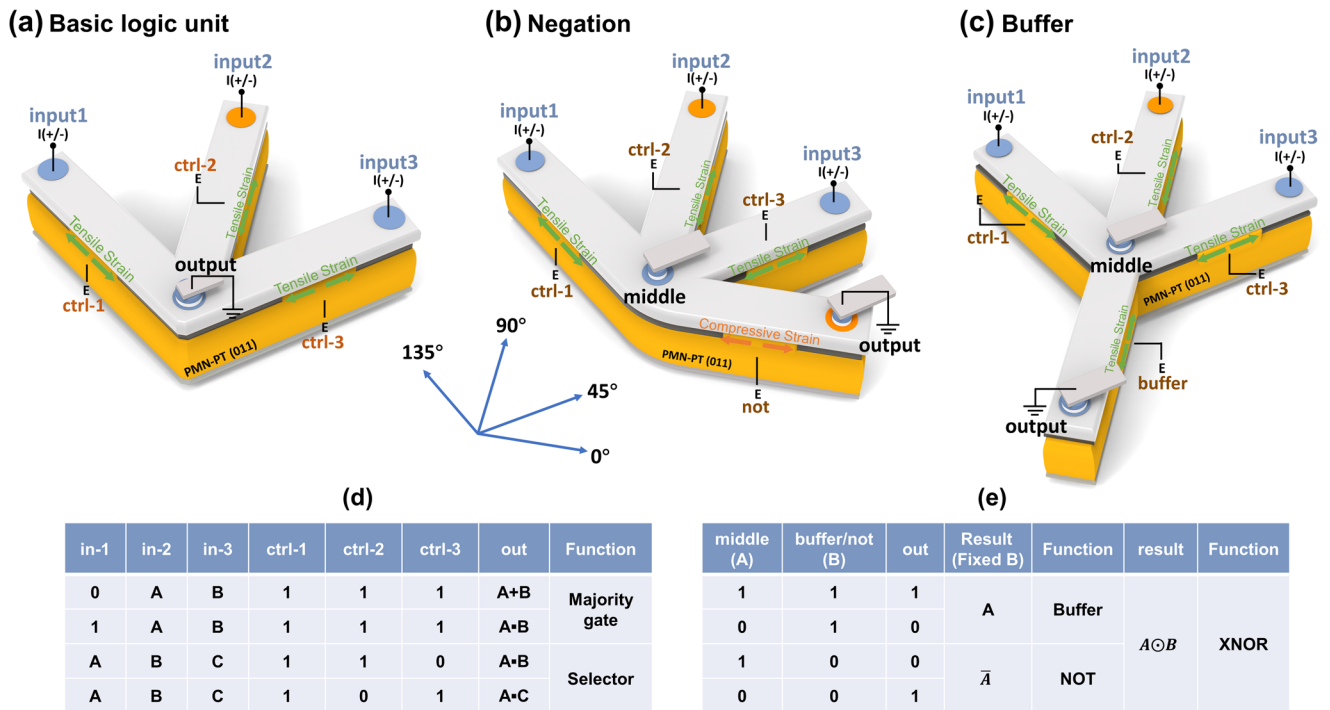
Fig. 4 | SOT on PMNPT based logic operations. a Single unit of majority gate device to implement and/or/selector logic functions. Implementations of data (**b**) negation and **c** buffering logic functions. **d**, **e** The truth tables for different operations.

middle end will be buffered/negated to the output end while in the "BUFFER" / "NOT" structure, respectively. In this way, BUFFER and NOT logic functions can be easily implemented. Corresponding logic settings of input/output and control arms (buffer/negation) are listed in the truth table shown in Fig. 4e. Cascading ability is also possessed in this logic device. Only when the electric field is power-on, the control arms can facilitate the transfer of magnetization state. Magnetic states of the outputs can be only transferred to the last unit without any influence on the inputs of the prior unit to achieve good non-reciprocity.

The device region can be customized by altering its parts through the use of different electric field configurations, resulting in corresponding strains that allow for an additional level of control. This enables the implementation of various logic functions such as "AND", "OR", and selector, within a single logic device. Moreover, cascading between logic units can be achieved using buffer and not operations, thereby enabling the implementation of complex logic functions. By utilizing electric field-induced strain, magnetization switching occurs at a lower current density via SOT technology, leading to a significant reduction in power consumption. The power consumed by the applied electric field is negligible. Our proposed electric-field assisted SOT device demonstrates remarkable potential to achieve complete Boole logic with extremely low power consumption and versatile reconfigurable structure; thus making it highly competitive compared to conventional SOT-based devices in terms of energy efficiency.

We have demonstrated the ability to quantitatively control magnetization switching in FM/HM/PMN-PT heterostructures by systematically investigating the angle dependence of the SOT effect. The localized in-plane strain on a piezoelectric substrate was precisely regulated through vertical DC electric field application across the substrate, allowing for accurate modulation of magnetization switching in SOT devices. Depending on device settings, the effective field of DLT decreased in 0-degree devices (under compressive strain) and increased in 45-, 90-, and 135-degree devices (under tensile strain), respectively, which could either impede or facilitate magnetization switching, respectively. This phenomenon was subsequently verified using MFM, XMCD-PEEM, as well as micromagnetic simulation techniques and

can be utilized to enhance low-power consumption performance in multiferroic logic devices.

Methods
Device fabrication
The Magnetic stack of heavy metal (HM)/ ferromagnet (FM) structure cap with a thin layer [Ta(5 nm)/CoFeB (3 nm)/Pt(1.5 nm)] is deposited with magnetron sputtering on (011) PMN-PT substrate (5 mm*5 mm*0.5 mm). The top and bottom of the PMN-PT substrate are capped with Pt (50 nm) and the magnetic stack is isolated from the top PMN-PT cap with AlOx 100 nm deposited with RF sputtering. First, the Hall bar structure of length 50um and width of 5um is patterned with optical lithography and ion milling. Later, Ti(10 nm)/Au(150 nm) contact pad is deposited with evaporation and Liftoff process.

VSM
A VSM 7400 from Lake Shore Cryotronics Inc. was used to perform conventional volume-averaging magnetometry measurements. The sample was mounted on a quartz holder and its magnetic moment was measured with the magnetic field from -1T ~ 1 T.

MFM
MFM measurements were conducted in a dynamic lift mode with a lift distance of 30 nm. The dynamics were measured by sweeping the field range in the presence of a magnetic field.

PEEM
XMCD-PEEM was used to image the magnetic state. The magnetic state in each magnetic layer was separately imaged by exploiting the probe depth of approximately 5 nm and the elemental sensitivity of X-ray absorption at the Co L_3-edges.

X-ray diffraction
Microdiffraction scanning collected individual diffraction patterns step by step from grid points to provide information on lattice strain and crystal orientation. The electrically induced deviatoric strain was calculated for each

step by taking the difference between the extracted strain at a non-zero voltage and at a zero voltage. The 2D strain maps were constructed with $10 \times 10 \ \mu m^2$ pixels.

Simulation

COMSOL and OOMMF were used for simulation in this work. The Structural Mechanics Module, Piezoelectric Module, and Magnetostrictive Module were added in COMSOL Multiphysics to analyze the strain and coupling between the piezoelectric substrate and FM thin film in the multiferroic heterostructure. The strain distribution on the FM layer was subsequently applied to the micromagnetic simulation toolkit OOMMF. The YY_FixedMEL: magnetoelastic term was used to calculate magnetoelastic energy based on the displacement field, in the form of Oxs VectorField[49]. The strain distribution obtained from COMSOL was transformed into a spatially correlated uniaxial anisotropy-like magnetoelastic energy, utilizing the magnetoelastic coupling constant consistent with that of the CoFeB film. Other key contributing terms of the effective magnetic field were uniaxial anisotropy, exchange coupling, and demagnetization. The FM layer ($300 \times 300 \times 1 \ nm^3$) was divided by the finite element method (FEM) with a mesh size of $3 \times 3 \times 1 \ nm^3$. Areas other than the FM bar and electrodes were vacuumed by setting $M_s = 0$. The saturation magnetization (M_s), exchange constant (A_{ex}), magnetic anisotropy energy density (K_u), spin polarization (p), and Gilbert damping constant (α) values used in this paper were 0.86×10^6 A/m, 30×10^{-12} J/m, 0.84 MJ/m^3, 0.6, and 0.014, respectively, for the FM layer, consistent with CoFeB-based FM material properties. Uniaxial anisotropy direction and initial magnetization direction were set along the longitudinal direction of the bar due to the shape anisotropy of in-plane magnetized film and demagnetization. Polarization direction of the spin current was perpendicular to the bar due to the spin hall effect.

References

1. Audia, P. G. & Goncalo, J. A. Past success and creativity over time: A study of inventors in the hard disk drive industry. *Manag. Sci.* **53**, 1–15 (2007).
2. Piramanayagam, S. N. Perpendicular recording media for hard disk drives. *J. Appl. Phys.* **102**, 011301 (2007).
3. Ripka, P. & Janosek, M. Advances in magnetic field sensors. *IEEE Sens. J.* **10**, 1108–1116 (2010).
4. Daughton, J. et al. Magnetic field sensors using GMR multilayer. *IEEE Trans. Magn.* **30**, 4608–4610 (1994).
5. Zidan, M. A., Strachan, J. P. & Lu, W. D. The future of electronics based on memristive systems. *Nat. Electron.* **1**, 22–29 (2018).
6. Xia, Q. & Yang, J. J. Memristive crossbar arrays for brain-inspired computing. *Nat. Mater.* **18**, 309–323 (2019).
7. Chowdhury, S., Datta, S., & Camsari, K. Y. A probabilistic approach to quantum inspired algorithms. In IEEE International Electron Devices Meeting (IEDM) (pp. 37–5) (IEEE, 2019).
8. Lee, O., You, L., Jang, J., Subramanian, V. & Salahuddin, S. Flexible spin-orbit torque devices. *App. Phys. Lett.* **107**, 252401 (2015).
9. Kobayashi, D. et al. Influence of heavy ion irradiation on perpendicular-anisotropy CoFeB-MgO magnetic tunnel junctions. *IEEE Trans. Nucl. Sci.* **61**, 1710–1716 (2014).
10. Campbell, V. E. et al. Engineering the magnetic coupling and anisotropy at the molecule–magnetic surface interface in molecular spintronic devices. *Nat. Commun.* **7**, 13646 (2016).
11. Shen, W. et al. Effect of film roughness in MgO-based magnetic tunnel junctions. *App. Phys. Lett.* **88**, 182508 (2006).
12. Heron, J. T. et al. Electric-field-induced magnetization reversal in a ferromagnet-multiferroic heterostructure. *Phys. Rev. Lett.* **107**, 217202 (2011).
13. Wang, J. B. N. J. et al. Epitaxial BiFeO$_3$ multiferroic thin film heterostructures. *Science* **299**, 1719–1722 (2003).
14. Spaldin, N. A. & Ramesh, R. Advances in magnetoelectric multiferroics. *Nat. Mater.* **18**, 203–212 (2019).
15. Trassin, M. Low energy consumption spintronics using multiferroic heterostructures. *J. Phys. Condens. Matter* **28**, 033001 (2015).
16. Vopson, M. M. Fundamentals of multiferroic materials and their possible applications. *Crit. Rev. Solid State Mater. Sci.* **40**, 223–250 (2015).
17. Hill, N. A. Why are there so few magnetic ferroelectrics? *J. Phys. Chem. B* **104**, 6694–6709 (2000).
18. Ramesh, R. & Spaldin, N. A. Multiferroics: Progress and prospects in thin films. *Nat. Mater.* **6**, 21–29 (2007).
19. Vaz, C. A. F. & Staub, U. Artificial multiferroic heterostructures. *J. Mater. Chem. C.* **1**, 6731–6742 (2013).
20. Gambardella, P. & Miron, I. M. Current-induced spin–orbit torques. *Philos. Trans. R. Soc. A: Math., Phys. Eng. Sci.* **369**, 3175–3197 (2011).
21. Qiu, X., Shi, Z., Fan, W., Zhou, S. & Yang, H. Characterization and manipulation of spin orbit torque in magnetic heterostructures. *Adv. Mater.* **30**, 1705699 (2018).
22. Sura, A., & Nehra, V. Performance comparison of single level STT and SOT MRAM cells for cache applications. In 2021 25th International Symposium on VLSI Design and Test (VDAT) (pp. 1-4). IEEE (2021)
23. Shao, Q. et al. Roadmap of spin–orbit torques. *IEEE Trans. Magn.* **57**, 1–39 (2021).
24. Ramaswamy, R., Lee, J. M., Cai, K. & Yang, H. Recent advances in spin-orbit torques: Moving towards device applications. *Appl. Phys. Rev.* **5**, 031107 (2018).
25. Song, C. et al. Spin-orbit torques: Materials, mechanisms, performances, and potential applications. *Prog. Mater. Sci.* **118**, 100761 (2021).
26. Miron, I. M. et al. Perpendicular switching of a single ferromagnetic layer induced by in-plane current injection. *Nature* **476**, 189–193 (2011).
27. Liu, L., Lee, O. J., Gudmundsen, T. J., Ralph, D. C. & Buhrman, R. A. Current-induced switching of perpendicularly magnetized magnetic layers using spin torque from the spin Hall effect. *Phys. Rev. Lett.* **109**, 096602 (2012).
28. Avci, C. O. et al. Fieldlike and antidamping spin-orbit torques in as-grown and annealed Ta/CoFeB/MgO layers. *Phys. Rev. B* **89**, 214419 (2014).
29. Peng, S. et al. Modulation of heavy metal/ferromagnetic metal interface for high-performance spintronic devices. *Adv. Electron. Mater.* **5**, 1900134 (2019).
30. Hayashi, M., Kim, J., Yamanouchi, M. & Ohno, H. Quantitative characterization of the spin-orbit torque using harmonic Hall voltage measurements. *Phys. Rev. B* **89**, 144425 (2014).
31. Zhang, X. et al. Electrical control over perpendicular magnetization switching driven by spin-orbit torques. *Phys. Rev. B* **94**, 174434 (2016).
32. Fukami, S., Anekawa, T., Zhang, C. & Ohno, H. A spin-orbit torque switching scheme with collinear magnetic easy axis and current configuration. *Nat. Nanotechnol.* **11**, 621–625 (2016).
33. You, L. et al. Switching of perpendicularly polarized nanomagnets with spin orbit torque without an external magnetic field by engineering a tilted anisotropy. *Proc. Natl Acad. Sci.* **112**, 10310–10315 (2015).
34. Eerenstein, W., Mathur, N. D. & Scott, J. F. Multiferroic and magnetoelectric materials. *Nature* **442**, 759–765 (2006).
35. Lei, N. et al. Strain-controlled magnetic domain wall propagation in hybrid piezoelectric/ferromagnetic structures. *Nat. Commun.* **4**, 1378 (2013).
36. Li, X. et al. Energy efficient all-electric-field-controlled multiferroic magnetic domain-wall logic. *Nano Lett.* **23**, 6845–6851 (2023).
37. Chen, A. et al. Full voltage manipulation of the resistance of a magnetic tunnel junction. *Sci. Adv.* **5**, 5141 (2019).
38. Chen, A. et al. Nonvolatile magnetoelectric switching of magnetic tunnel junctions with dipole interaction. *Adv. Funct. Mater.* **33**, 2213402 (2023).
39. Li, P. et al. Electric field manipulation of magnetization rotation and tunneling magnetoresistance of magnetic tunnel junctions at room temperature. *Adv. Mater.* **25**, 4320–4325 (2014).

40. Chen, A. et al. Giant nonvolatile manipulation of magnetoresistance in magnetic tunnel junctions by electric fields via magnetoelectric coupling. *Nat. Commun.* **10**, 243 (2019).
41. Filianina, M. et al. Electric-field control of spin-orbit torques in perpendicularly magnetized W/CoFeB/MgO films. *Phys. Rev. Lett.* **124**, 217701 (2020).
42. Cai, K. et al. Electric field control of deterministic current-induced magnetization switching in a hybrid ferromagnetic/ferroelectric structure. *Nat. Mater.* **16**, 712–716 (2017).
43. Kim, J. et al. Layer thickness dependence of the current-induced effective field vector in Ta| CoFeB| MgO. *Nat. Mater.* **12**, 240–245 (2013).
44. Avci, C. O. et al. Interplay of spin-orbit torque and thermoelectric effects in ferromagnet/normal-metal bilayers. *Phys. Rev. B* **90**, 224427 (2014).
45. Donahue, M. J. & Porter, D. G. OOMMF User's Guide, version 1.0 (1999).
46. Liu, Y. T. et al. Anatomy of Type-*x* Spin-orbit-torque switching. *Phys. Rev. Appl.* **16**, 024021 (2021).
47. Xue, F. et al. Field-free spin-orbit torque switching assisted by in-plane unconventional spin torque in ultrathin [Pt/Co]N. *Nat. Commun.* **14**, 3932 (2023).
48. Biswas, A. K., Ahmad, H., Atulasimha, J. & Bandyopadhyay, S. Experimental demonstration of complete 180 reversal of magnetization in isolated Co nanomagnets on a PMN–PT substrate with voltage generated strain. *Nano Lett.* **17**, 3478–3484 (2017).
49. Yahagi, Y., Harteneck, B., Cabrini, S. & Schmidt, H. Controlling nanomagnet magnetization dynamics via magnetoelastic coupling. *Phys. Rev. B* **90**, 140405 (2014).

Author contributions
J.H. and L.X. wrote the main manuscript text and L.X. and H.S. prepared figures 1–4. All authors reviewed the manuscript.

Competing interests
The authors declare no competing interests.

Additional information
Correspondence and requests for materials should be addressed to Jeongmin Hong.

Reprints and permissions information is available at http://www.nature.com/reprints

Publisher's note Springer Nature remains neutral with regard to jurisdictional claims in published maps and institutional affiliations.